THE ASTROPHYSICAL JOURNAL, 400:638–646, 1992 December 1


# SPECTROSCOPY OF THE COMPANION AND BOW-SHOCK NEBULA OF PSR 1957+20

THOMAS L. ALDCROFT AND ROGER W. ROMANI
Department of Physics, Stanford University, Stanford, CA 94305-4060
AND
JAMES M. CORDES
Astronomy Department, Cornell University, Ithaca, NY 14853-6801
*Received 1992 April 15; accepted 1992 May 15*

## ABSTRACT

We have obtained moderate-resolution spectra of the bow-shock nebula and companion of the eclipsing binary pulsar PSR 1957+20. These data give us a measurement of the nebular Balmer decrement and emission-line strengths and establish that the emission is due to a nonradiative shock. We have developed a computational model of the nebular emission that we fitted to the observed spectra to obtain a kinematic estimate of the system distance and the local ISM conditions. We have also isolated the spectrum of the pulsar companion and follow its variation with the orbit. A lack of strong emission lines poses further problems for companion ablation with rapid thermally driven wind; the $\sim$1.2 kpc distance indicated by our analysis suggests instead that the companion is bloated to near Roche-lobe contact.

*Subject headings:* binaries: close — binaries: eclipsing — pulsars: individual (PSR 1957+20) — shock waves

## 1. INTRODUCTION

The discovery of the first eclipsing binary millisecond pulsar PSR 1957+20 (Fruchter, Stinebring, & Taylor 1988) provided a crucial link in our understanding of the evolution of low-mass X-ray binaries and millisecond period, "recycled" pulsars. In particular, observations indicated that some component of the pulsar's rotation-powered radiation is heating and ablating the companion—in apparent confirmation of predicted evolutionary scenarios (Ruderman, Shaham & Tavani 1989; Kluzniak et al. 1988). Optical detection of the $\lesssim 0.02\ M_\odot$ companion (Kulkarni, Djorgovski, & Fruchter 1988) confirmed this basic picture and measurements of the companion's colors and variability (Djorgovski & Evans 1988, hereafter DE; van Paradijs et al. 1988) place important constraints on models of the system. These data show that the companion is brightest at pulsar anti-eclipse, directly demonstrating the effect of the adjacent pulsar through heating of the companion surface and excitation of a stellar wind. There has been extensive discussion of the energization of this wind (e.g., Phinney et al. 1988); however, the mechanisms powering the observed wind, the physical conditions near the stellar surface, and the ability of the pulsar to carry the evaporation to completion are still unclear (see Levinson & Eichler 1991, and references therein).

In addition to the direct heating of the companion, another remarkable manifestation of the rotational energy lost in the spin-down of this 1.6 ms pulsar has been discovered by Kulkarni & Hester (1988, hereafter KH)—an H$\alpha$ nebula is being excited by interaction of the relativistic wind from the pulsar with neutral hydrogen in the surrounding interstellar medium (ISM). The rapid motion of the pulsar through the ISM, confirmed by high-precision timing studies (Ryba & Taylor 1992), causes this nebula to be drawn out in a cometary bow shock shape. Spectra of the nebula obtained by KH show a lack of metal forbidden lines, which suggests that emission arises from a collisionless nonradiative shock propagating into a partly neutral medium. However, an apparently very large Balmer decrement (H$\alpha$/H$\beta \gtrsim 12$) complicates this interpretation of the shock physics.

Because of the faintness of the companion ($m_V \approx 20$, at maximum) and the peculiarities of the nebular spectrum, higher sensitivity and higher resolution spectra are of particular importance in deciphering the nebular shock physics and the interaction of the pulsar wind with the companion surface. In addition, if any spectral signature from the ablating companion can be identified, it would provide an important means of measuring the mass of the recycled pulsar, which has evidently experienced substantial mass accretion. Such data are crucial for understanding pulsar recycling and the evolution of neutron star magnetic fields (Romani 1990).

## 2. OBSERVATIONS AND REDUCTIONS

We have acquired moderate-resolution, long-slit spectra of PSR 1957+20's binary companion and the surrounding bow shock pulsar wind nebula using the Double Spectrograph (Oke & Gunn 1982) at the Cassegrain focus of the Hale 5 m reflector at Palomar Observatory. The data were obtained during 1991 July 13–14 UT with a 1″ slit at a constant position and angle (after adjustment following initial exposures) oriented roughly along the minor axis of the bow shock (perpendicular to the inferred pulsar velocity). Repeated spectra were acquired with a dichroic filter (5500 Å) behind the slit to provide spectra in blue (4630–5070 Å; 1200 lines mm$^{-1}$ grating, 5000 Å blaze, first order) and red (6310–6960 Å; 1200 lines mm$^{-1}$ grating, 7100 Å blaze, first order) wavelength ranges. The two TI CCDs deliver data at 0.55 Å pixel$^{-1}$ and 0.81 Å pixel$^{-1}$, respectively, while the spatial dispersion along the slit was 0.″59 pixel$^{-1}$ in each camera. The good wavelength resolution, repeated observations and constant slit angle were designed to provide good signal-to-noise data on the nebula, to allow full coverage of the companion spectral variations during its 9.2 hr binary orbit and to allow good subtraction of a close ($\sim$0.″7 separation) faint G-star known to contaminate the spectrum of PSR 1957+20's companion. Seeing was good ($\lesssim$1.″5) through-

TABLE 1

JOURNAL 200″ DOUBLE SPECTROGRAPH OBSERVATIONS

| UT Midpoint (1991) | Orbital phase[a] | Exposure (s) | P.A.[b] | Comments |
|---|---|---|---|---|
| Jul 13, 05:09 | 0.37 | 1800 | 67° | Pulsar partly off slit |
| Jul 13, 05:38 | 0.43 | 1800 | 67 | Pulsar partly off slit |
| Jul 13, 06:10 | 0.49 | 1800 | 67 | Pulsar partly off slit |
| Jul 13, 06:46 | 0.55 | 1800 | 78 | ... |
| Jul 13, 07:42 | 0.64 | 3600 | 78 | ... |
| Jul 13, 08:48 | 0.76 | 3600 | 78 | ... |
| Jul 13, 09:55 | 0.90 | 3600 | 78 | ... |
| Jul 13, 10:58 | 0.01 | 3600 | 78 | ... |
| Jul 13, 11:38 | 0.08 | 917 | 78 | ... |
| Jul 14, 04:44 | 0.95 | 3600 | 78 | Red camera frost |
| Jul 14, 05:48 | 0.06 | 3600 | 78 | Red camera frost |
| Jul 14, 06:53 | 0.18 | 3600 | 78 | Red camera frost |
| Jul 14, 07:56 | 0.30 | 3600 | 78 | Red camera frost |
| Jul 14, 09:11 | 0.43 | 3600 | 78 | Red camera frost |
| Jul 14, 10:14 | 0.55 | 3600 | 78 | Red camera frost |
| Jul 14, 11:16 | 0.66 | 3600 | 78 | Red camera frost |

[a] Based on ephemerides in Ryba & Taylor 1992.
[b] Position angle, measured counterclockwise from pulsar velocity.

out the two nights of observation and improved to subarcsecond conditions for much of 1991 July 17. A log of the PSR 1957+20 exposures is given in Table 1. The time and binary orbital phase are given at the midpoint of each exposure.

In addition to the spectroscopy, a short exposure continuum image of the PSR 1957+20 field was taken with the 4-shooter camera on 1991 July 15; measurements on this image were used to accurately establish the position angle of the double spectrograph slit. The list geometry with respect to the pulsar proper motion and the positions of the field stars in the slit are indicated schematically in Figure 1.

The data were reduced using IRAF following standard two-dimensional spectral reduction procedures. Multiple comparison lamp spectra (Ne, red; FeAr, blue) were fitted with a low-order polynomial to provide wavelength calibration stable to ~0.2–0.3 Å over both the red and blue spectral ranges. Exposures of the spectrophotometric standards BD +17°4708 and BD +26°2606 (Gunn & Oke 1983) were used to flux calibrate the data; standard KPNO extinction corrections were applied in the reduction. Note that constraints on the slit position meant that we could not follow the parallactic angle during the observations. Also, the absence of flux calibration points at the very end of our spectral ranges causes appreciable error in the absolute fluxes at the edges of our spectra. Nevertheless, accounting for these effects and variable slit losses, we estimate a ~20% accuracy for our absolute spectrophotometry. During the second night of observations, there was a substantial and progressive loss of sensitivity in the red camera, as ascertained from the standard star fluxing. This is apparently due to growth of a layer of frost on the CCD window, as sometimes occurs when the red camera is kept cold for multinight runs. We accounted for this time-dependent decrease in the sensitivity by fitting a linear function of time (at each wavelength) to the sensitivity functions derived from the standard stars. Using this time-dependent calibration we found that the Hα flux was constant and agreed with the flux observed in the data from the first night. This indicates that stable and accurate flux calibration was restored. The substantial decrease in signal to noise, however, means that many of our "red wavelength" results are based primarily on data from 1991 July 13; the blue camera was not affected.

## 3. SPECTROSCOPY OF THE BOW SHOCK NEBULA

In Figure 2 we show the blue and red nebular spectra, integrated over the bright eastern limb of the pulsar's bow shock nebula. The spectra have been normalized to the flux in Hα. We see that Hα and Hβ are clearly well detected, but the nebular lines of heavier species are not detected at a 3 σ confidence level. Due to a lack of comparison fluxes on the standard stars, the flux normalization is somewhat uncertain in the extreme ~50 Å of each spectrum; also the telluric $O_2$ band above 6870 Å has not been fully removed. Additional night sky features are indicated above the spectrum along with the positions of several typically strong nebular lines.

We have determined conservative upper limits on line strengths as 3 times the standard deviation in the continuum regions of the spectra. For unresolved nebular lines these limits correspond to 3.5% of the Hα flux in the red and 16% of the Hβ flux in the blue. This Balmer dominance is a strong signature of a nonradiative shock in a partly neutral medium. Comparison with the results of Raymond et al. (1980, 1983) for the Cygnus loop shows that the Balmer domination of the PSR 1957+20 nebula is very strong; for example, in the latter work observed ratios of He II λ4686/Hβ = 0.24 and [O III] λ5007/Hβ = 0.14 were found. Our conservative upper limits are comparable to or lower than these values, and accordingly in better agreement with nonradiative shock models. We suggest that

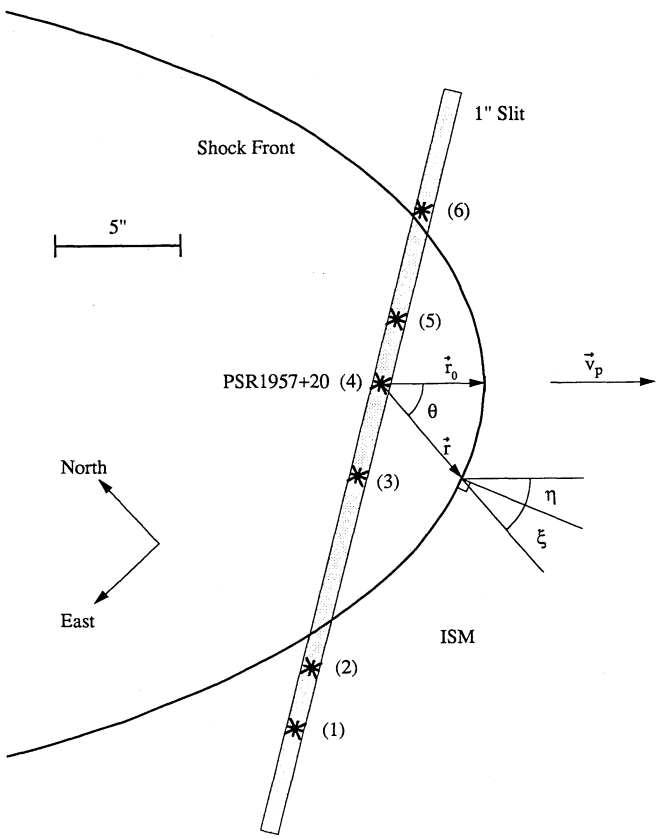


FIG. 1.—Geometry of our PSR 1957+20 observations and of the bow shock shape calculation; see text. The stars in the slit which are labeled (1)–(6) correspond to the continuum peaks shown in Fig. 3.

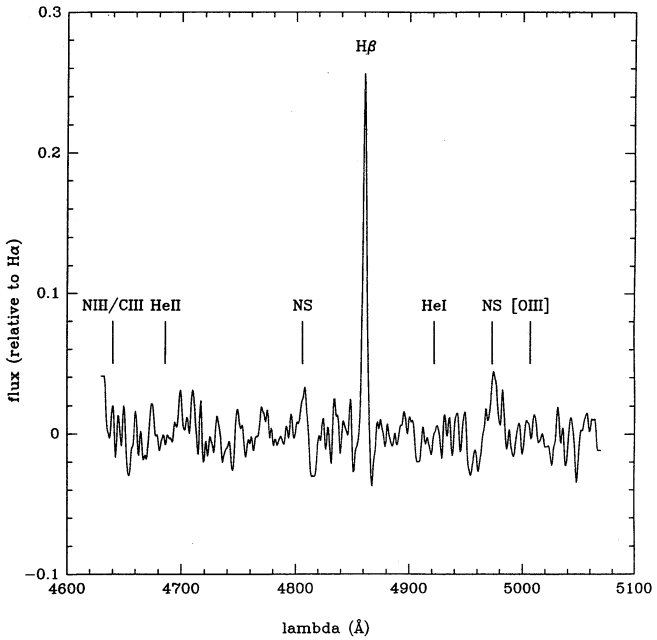


FIG. 2a

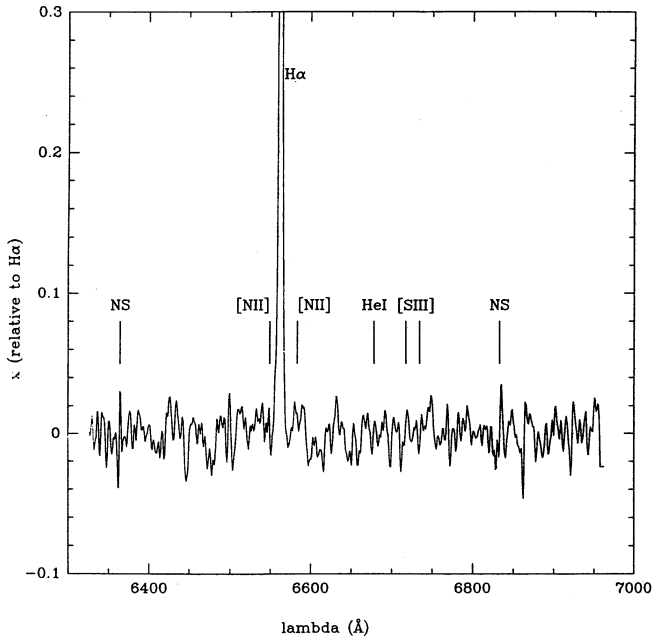


FIG. 2b

FIG. 2.—Optimally extracted spectra of bow shock nebula around PSR 1957+20. Fluxes normalized to Hα. Typically strong nebular emission lines are marked, along with imperfect night sky subtraction (NS). (*a*) Blue camera spectrum. (*b*) Red camera spectrum.

the differences may be due to a neutral fraction in the incoming ISM higher than the ~30% estimated for the Cygnus Loop as well as the higher velocity of the postshock flow in the PSR 1957+20 system.

Using various positions across the nebula we have made local determinations of the Balmer decrement (Hα/Hβ flux ratio). At the bright left (eastern) limb of the nebula, an integration over nine spatial pixels gives a value $H\alpha/H\beta = 3.5 \pm 0.4$, while towards the center of the nebula, where the nebular shocks are viewed more nearly face-on, we measure $H\alpha/H\beta = 3.3 \pm 0.5$. We are careful to avoid pixels for which continuum flux shows stellar contamination; in particular, the right (western) limb-brightened edge of the nebula is not included, due to the presence of a bright star with a strong Balmer absorption near that position. The average Hα/Hβ flux ratio measured is $3.5 \pm 0.5$, where the error estimate comes both from variations in values in subsets of the data and expected errors in the relative spectrophotometry. This value is in good agreement with estimates for slow nonradiative shocks (Raymond 1991) and its low value indicates a small visual absorption $A_V \lesssim 1$ mag. This limit is consistent with the exclusion of high $A_V$ on energetic grounds (DE). Our limit also agrees with the expected $A_V$ based on the ~1 kpc pulsar distance estimated from its dispersion measure DM = 29 cm$^{-3}$ pc. We will make more detailed comment on the implications for the shock physics and the companion status in § 6.

The Hα line profile that we measure from the data is clearly substantially wider than the instrumental spectral resolution of the red camera observations ($\sigma = 1.1$ Å = 52 km s$^{-1}$). In Figure 3 we show the results of a single Gaussian fit to the Hα line as a function of position across the nebula. The limb-brightened nebula shows clearly in the flux curve ($I_{H\alpha}$), where the right edge is somewhat affected by the absorption in a field star. We also see that the velocity width ($\sigma_{H\alpha}$) of the emission varies strongly with position. Near the nebula edges it is consistent with the instrumental resolution, while near the pulsar position (where the nebular shock flows have substantial line-of-sight velocities) the width is $\sigma \sim 120$ km s$^{-1}$. The mean velocity ($\langle v_{H\alpha} \rangle$) shows a modest ~25 km s$^{-1}$ variation across the nebular emission. The Hβ observations also suggest a profile slightly broader than the instrumental resolution, but the signal to noise are insufficient to derive quantitative results.

## 4. BOW SHOCK MODELS AND SYSTEM PARAMETERS

### 4.1. *Bow Shock Physics*

The imaging data (KH) show a strongly edge-brightened nebula with a classic cometary bow-shock shape. The inference is that the luminosity radiated from the pulsar spin-down in the form of relativistic particles and fields shocks against the external ISM. The shocked mass, which is dominated by the contribution from the ISM, is then swept back by the pulsar's substantial proper motion. The absence of forbidden lines and the sharp limb-brightened nebular edge indicate that the emission layer is thin and nonradiative. We believe that this condition obtains in this case because of the large velocities along the shock front caused by the pulsar's motion, which carry the postshock gas to the tail of the nebula before it can cool. As this material cools downstream recombination radiation should be emitted. This may account for the extensive and patchy Hα emission seen at large distances behind the pulsar in the images of KH. We would anticipate that the emission in some of these regions, as well as perhaps that near the stagnation point at the nose of the bow shock, will exhibit a spectrum of radiative shock emission, in contrast to the spectra we have observed.

The surface brightness and emission line profile of the nebular emission depend on the shock physics. Nonradiative shock emission has been recently reviewed by Raymond (1991), and we mention only the most pertinent features here. As the

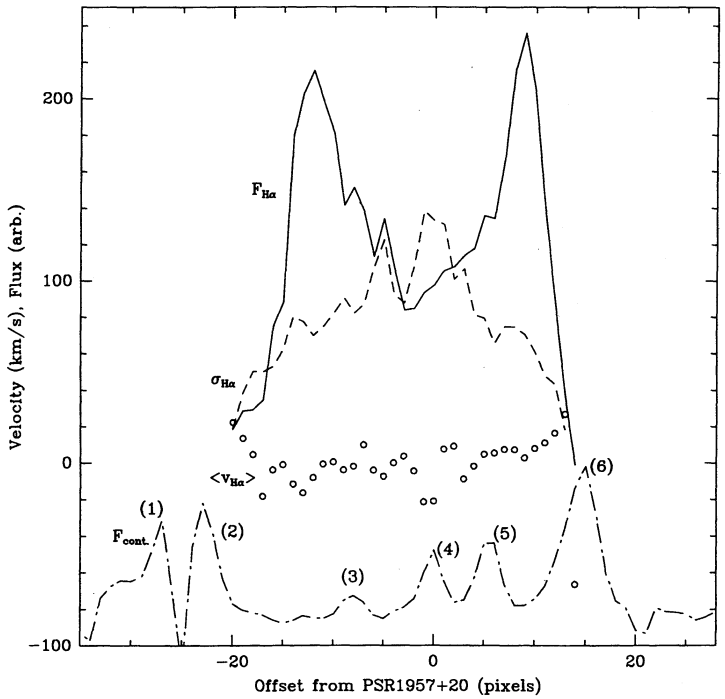


FIG. 3.—Single Gaussian fit to the nebular Hα line profile as a function of pixel offset from PSR 1957+20 along the slit. *Solid line:* Hα (arbitrary units). *Dashed line:* Gaussian line width (km $s^{-1}$). *Dotted line:* Central line velocity (km $s^{-1}$). *Dot-dashed line:* continuum flux, i.e., stellar contamination (arbitrary units, stars are labeled as in Fig. 1).

bow wave sweeps up the partly neutral medium, the collisionless shock rapidly thermalizes the kinetic energy of the ionized fraction of the interstellar medium, while the neutral fraction passes freely into the hot postshock gas. Thus we have neutral atoms embedded in a medium with ion temperature $T_i \sim 10^6$ K and electron temperature $T_e \sim 10^4$ K. Note that the electron temperature equilibration time is rather controversial, but may approach the (long) Coulomb time scale in the postshock flow. In the postshock environment the neutral atoms can suffer both collisional excitation and ionization. Thus before the neutrals are ionized and are rapidly accelerated to join the postshock flow of the charged species, there is a thin $\sim 10^{16}$ cm region for which collisional excitation causes de-excitation radiation. This emission will give a narrow line ($\lesssim 10$ km $s^{-1}$) at the preshock temperature and the ISM line-of-sight velocity $v_0$. In addition, resonant charge exchange between the slow postshock neutrals and the fast ions causes a population of neutrals at the postshock bulk velocity and temperature to build up in the shock flow. These also emit Balmer photons, both in returning to the ground state and through subsequent collisional excitation.

The slow and fast populations of neutral atoms thus cause the emission line profile of a given piece of the nebula to show narrow and velocity-shifted broad-line components (with fluxes $I_N$ and $I_B$, respectively); the narrow to broad flux ratio is expected theoretically to be somewhat less than unity. Excitation, charge exchange and ionization are all collisional processes here, so we expect that the emission will be confined to a layer of approximately constant column density (along the pulsar velocity) in the bow-shocked gas. The velocity and temperature dependencies of the collisional cross sections will cause some variation across the surface that we can ignore at present accuracy. This gives a constant emissivity of $\sim 0.2$ Hα photons per incoming neutral, so that the changing aspect ratio that the bow shock presents to the incoming ISM flow causes the surface brightness of the nebula to vary as $\cos \eta$ (see Fig. 1). We expect downstream radiative recombinations will cause some departure from this law.

### 4.2. *Kinematic Model*

From the discussion in the previous section it is clear that spectroscopy at sufficiently high resolution can provide a wealth of information on the shock physics and the pulsar environment. Encouraged by our preliminary analysis in § 3, we have constructed a kinematic model of the pulsar bow shock nebula to be compared directly with our spectroscopy and qualitatively with preexisting imaging data.

The position of the contact discontinuity between the shocked pulsar wind and the shocked ISM can be determined by momentum balance (for a thin shock this gives the position of the nonradiative shock front). If the shocked nebular material has a surface mass density $\Sigma$, then for a pulsar with a spindown luminosity $\dot{E}$, moving through an external medium of density $\rho$ at velocity $\boldsymbol{v}_p$, the momentum balance condition is

$$(\rho v_p \cos \eta) v_p \cos \eta = \frac{\dot{E}}{4\pi c r^2} \cos^2 \xi + \frac{\Sigma v_t^2}{R} . \quad (1)$$

The last term accounts for the centrifugal force on the postshock material flowing along the nebular surface (Baranov et al. 1971). Here $\boldsymbol{v}_t$ is tangential velocity of the bulk postshock flow, $\eta$ is the angle between $\boldsymbol{v}_p$ and the normal to the nebula surface, $\xi$ is the angle between this normal and the direction to the pulsar, and $R$ is the local radius of curvature of the nebula surface in the plane containing $\boldsymbol{v}_t$ (see Fig. 1).

Since for a homogeneous external medium the shock front will be a surface of revolution about the pulsar velocity axis, we can solve for the shape of the shell as $r(\theta)$, where $\theta$ measures the angle from this axis. First, we note that $2\pi r \sin\theta \Sigma v_t \equiv \dot{m}$, the mass flow along the shell, and $\dot{m}v_t$ is the tangential momentum flux in this surface at a position $r(\theta)$. So we have

$$\dot{m}v_t = 2\pi r \sin\theta R\left(\rho v_p^2 \cos^2\eta - \frac{\dot{E}}{4\pi c r^2}\cos^2\xi\right)$$

$$= 2\pi\rho v_p^2 r \sin\theta R\left[\cos^2\eta - \left(\frac{r_0}{r}\right)^2 \cos^2\xi\right], \quad (2)$$

where $r_0 \equiv [\dot{E}/(4\pi c\rho v_p^2)]^{1/2}$ is the characteristic length scale and from equation (1) is, in fact, the standoff distance of the contact discontinuity at the nose where $\theta = \eta = \xi = v_t = 0$. In the shock frame momentum is added to the material at a rate per unit shock area of

$$\frac{d(\dot{m}v_t)}{dA_{\rm sh}} = (\rho v_p \cos\eta)v_p \sin\eta + \frac{\dot{E}}{4\pi c r^2}\cos\xi\sin\xi$$

$$= \rho v_p^2 \frac{[\sin 2\eta + (r_0/r)^2 \sin 2\xi]}{2}, \quad (3)$$

where the shock front area is $dA_{\rm sh} = 2\pi r \sin\theta[r^2 + (dr/d\theta)^2]^{1/2} d\theta$. From the derivative of equation (2), we write

$$\pi r \sin\theta\left[\sin 2\eta + \left(\frac{r_o}{r}\right)^2 \sin 2\xi\right] = \frac{1}{(r^2 + r'^2)^{1/2}}$$

$$\times \left\{2\pi r \sin\theta R\left[\cos^2\eta - \left(\frac{r_0}{r}\right)^2 \cos^2\xi\right]\right\}', \quad (4)$$

where the derivatives are taken with respect to $\theta$. Since $\xi = \text{atan}(r'/r)$, $\eta = \theta - \xi$ and $R = (r^2 + r'^2)^{3/2}(r^2 + 2r'^2 - rr'')^{-1}$, we can solve equation (4) for a third-order differential equation in $r(\theta)$. The first required boundary condition comes from equation (1) and gives $r(0) = r_0$; the second comes from symmetry at the "nose" of the bow shock, so that $r'(0) = 0$. The integrand in the differential equation is a singular quotient—expanding the numerator and denominator in a Taylor series about the origin to order $\theta^4$ allows us to solve for the roots $r''(0)$ which make the singularity integrable. With the resulting additional boundary condition $r''(0) = r_0/2$ we have integrated this differential equation with a Runge-Kutta algorithm to derive $r(\theta)$, the shape of the bow-shock nebula. This is shown in Figure 1. The shape is in agreement with similar calculations by other authors (Baranov et al. 1971; Mac Low et al. 1991; Van Buren & Mac Low 1992), although our computational technique and emission zone physics are quite different. For instance, the latter authors have used a finite element technique to solve for the shape and velocity structure of bow-shock nebulae of ultracompact H II regions around young stars.

We can now compute the bulk flow velocity along the bow-shock surface. Noting that the surface mass density is dominated by the ISM contribution and that all mass swept up at angles less than $\theta$ must flow along the surface at $r(\theta)$, we see that

$$\dot{m}(\theta) = \pi(r\sin\theta)^2 \rho v_p .$$

From equation (2) this gives

$$v_t = \frac{2v_p R}{r\sin\theta}\left[\cos^2\eta - \left(\frac{r_o}{r}\right)^2\cos^2\xi\right]. \quad (5)$$

The surface density then follows from $\Sigma = \dot{m}/(2\pi r v_t \sin\theta)$.

Pulse timing observations give us precise measurements of several of the physical quantities in our model. From the results of Ryba & Taylor (1992) the pulsar period (1.607 ms) and period derivative ($1.68 \times 10^{-20}$) give the spin-down luminosity of PSR 1957+20 as $\dot{E} = 1.6 \times 10^{35} I_{45}$ ergs s$^{-1}$, where the pulsar moment of inertia $I_{45}$ is in units of $10^{45}$ g cm$^2$. In addition, timing proper-motion measurements give the transverse velocity of the pulsar. If this velocity vector is at an angle $i$ to the plane of the sky and the pulsar is at a distance $d_{\rm kpc}$ kiloparsecs, then the space velocity of PSR 1957+20 is determined to be $v_p = 1.38 \times 10^7 d_{\rm kpc}/\cos i$ cm s$^{-1}$. With these values we can estimate the angular distance of the contact discontinuity standoff in a medium of baryon number density $n_0$ cm$^{-3}$ as $\alpha = 2\farcs5 I_{45}^{1/2} \cos i/(d_{\rm kpc}^2 n_0^{1/2})$. For a nonradiative shock, the observed Hα emission, however, comes from immediately behind the shock front itself. We can estimate the additional standoff distance $h$ by balancing the gas pressure in the postshock flow with the ram pressure of the ISM. In the postshock shell $kT$ is $(2/3\dot{U})/\dot{N}$, where $\dot{U}$ and $\dot{N}$ are the rates of postshock internal energy and particle number flow through the shell, respectively. Near the nose of the shock, $N = nA_{xs}v_f$, where the flow velocity is $v_f \approx v_p \sin(\eta)$ and the transverse cross-sectional area of the shell at an angle $\theta$ is $A_{xs} = \pi[(r + h)^2 - r^2]\cos\xi\sin\theta\sin\eta$. There we also have $\xi = \tan^{-1}[(r + h)'/(r + h)] \approx \tan^{-1}[r'/(r + h)]$, and the thermalized kinetic energy swept up out to $\theta$ gives $\dot{U} = (\pi/2)\rho v_p^2 (r + h)^2 \sin^2\theta$. With these estimates, we set $P_{\rm gas} = nkT = P_{\rm ram} = \rho(v_p \cos\eta)^2$ and solve iteratively for the shocked ISM thickness, finding $h = 0.34 r_0$. Accordingly we derive the standoff distance of the shock Hα emission as

$$\beta = 3\farcs3 I_{45}^{1/2} \cos i/(d_{\rm kpc}^2 n_0^{1/2}), \quad (6)$$

which may be compared with the observed value of ~4″ (KH) after allowing for seeing. We will assume that $I_{45} = 1$, and our modeling below shows that $i$ is small, so this observation indicates that the swept-up medium has a density of $n_0 \sim 0.7 d_{\rm kpc}^{-4}$. For solar abundances, the corresponding hydrogen density is $\sim 0.5 d_{\rm kpc}^{-4}$ cm$^{-3}$. The angular scale of the emission line profile along the slit gives a similar constraint from our data.

We should also check that our nonradiative shock condition is valid, i.e., that the flow time $t_{\rm fl} \sim r_0/v_p$ is less than the cooling time for the shocked gas, $t_c \sim 10^{11} v_7^{3.2}/n_0$ s (McKee & Hollenbach 1980), where $v_7$ is the flow velocity in units of $10^7$ cm s$^{-1}$. Assuming $\cos i = 1$ and using the observed proper motion and nebula size to eliminate the density and velocity in favor of the distance, the condition that the postshock avoid cooling is $d_{\rm kpc}^{7.2} \gtrsim 8 \times 10^{-3}$. Thus for $d_{\rm kpc} \approx 0.5$ the shock remains nonradiative and for slightly larger distances this condition is very well satisfied. We have integrated a one-zone model of thermal pressure balance against the oncoming ISM along the postshock layer to follow the variation in $h$ as the ram pressure drops and the mean energy per particle decreases due to adiabatic losses and dilution with more weakly shocked gas. We find that $h/r$ remains roughly constant, until well downstream; the true behavior will depend on the details of the postshock flow, but it is adequate to hold $h/r$ constant at the computed value in our modeling below.

Because the nonradiative line flux arises in the immediate postshock flow, it will not trace the bulk transverse velocity of equation (5) unless there is rapid mixing. Instead, we apply the jump conditions locally at the strong shock front to find that the Hα emission arises from a region with a tangential velocity $v_{\parallel} = v_p \sin\eta$ and a normal velocity $v_{\perp} = v_p(\cos\eta)/4$ in the

bow-shock frame. This is projected onto the line of sight and convolved with a velocity spread given by the thermalized kinetic energy with $\sigma = (5/8)^{1/2} v_p \cos \eta$ to give the local contribution to the shock line profile.

Equation (6) gives three of the free parameters in the kinematic model: $i$, $n_0$, and $d_{\rm kpc}$. The remaining parameters, introduced in § 4.1, are $f_b$ (the fraction of the total line emission in the broad component) and $v_0$ (the line-of-sight bulk velocity of the ISM). From our astrometry and the continuum flux in the slit we determine the slit to be at an angle of 78° (measured north through east) from the projected pulsar velocity measured by Ryba & Taylor. A model two-dimensional spectrum of the nebula's Hα emission is computed by a projection along this slit of the surface of revolution defined by $r(\theta)$ for the given set of the parameters. This is then convolved with the instrumental resolution profiles as determined in the wavelength direction from measurements of arc lines and night sky lines near Hα and in the spatial dimension from stellar profiles near the nebular position. We normalize this kinematic model to the observed integrated line flux to compare with the data. We note that this normalization and the fraction $f_b$ are in principle set by the shock physics for the parameters $n_0$ and $v_p(d_{\rm kpc}, i)$; although we do not infer these directly, the measured values are in accord with estimates for the expected values and are constant in the observed spectral slice.

We have streamlined this two-dimensional spectrum calculation and wedded it to a simulated annealing algorithm (Press & Teukolsky 1991) for model fitting in this multidimensional parameter space. The result of this computational comparison with the data are best-fit values for the physical parameters of the 1957+20 system. These values are given in Table 2, where the errors give the ranges which cause a 10% increase in the likelihood function given by the summed squares of the fit residuals, *with the other parameters held fixed*. However, it is important to note that there are substantial covariances among several of these parameters and the unconstrained errors are in some cases larger. In particular, since the bow wave width is a strong constraint, scaling as equations (6), there is a large correlation between $d_{\rm kpc}$ and $n_0$. The spatial shape and asymmetry of the nebula cross section give the best constraint on the inclination angle. The individual determination of the distance and density are driven by the relatively small, although well resolved, velocity width near the nebular midpoint. Accordingly, the precision of this measurement depends on $f_b$, which is the fraction of the line in the velocity-broadened component. At the minimum theoretically expected value, $f_b = \frac{2}{3}$ (i.e., $I_b/I_n = 2$) given by Raymond (1991) the best-fit distance is 0.9 kpc; the fit degrades by 10% at 0.92 kpc and by 20% at 0.94 kpc. A somewhat better fit can actually be found for smaller values of $f_b$. At the global best-fit parameters, with $f_b = 0.4$, the fitted distance is 1.2 kpc; we prefer this value since, in fact, $f_b \approx 0.5$ is often observed in nonradiative shocks. Finally, varying $d_{\rm kpc}$ and $n_0$ together allow distances as large as $d_{\rm kpc} = 1.5$ with a 10% increase in the summed squared model residual; the unconstrained error in $d_{\rm kpc}$ is roughly $\pm 0.2$.

TABLE 2

PSR 1957+20 System Parameters

| Parameter | Best Fit | Fit with $f_b = \frac{2}{3}$ |
|---|---|---|
| $i$ ..... | $-4.3 \pm 5°$ | $-3.2^{+3.5}_{-4}°$ |
| $v_0$ ..... | $0^{+4}_{-1}$ km s$^{-1}$ | $0^{+4}_{-1.5}$ km s$^{-1}$ |
| $n_0$ ..... | $0.41 \pm 0.02$ cm$^{-3}$ | $1.39 \pm 0.02$ cm$^{-3}$ |
| $d_{\rm kpc}$ ..... | $1.2 \pm 0.01$[a] | $0.9 \pm 0.02$[a] |
| $f_b$ ..... | $0.4 \pm 0.2$ | $\frac{2}{3}$ (fixed) |

[a] Unconstrained errors ~0.2.

In Figure 4 we display the position-position (image) and position-velocity (spectral) model for the best-fit parameters above. To generate the image, for a given viewing angle and set of ISM conditions we employ a rapid ray tracing computation that determines the intersection with the nebula surface and the projected aspect of the postshock layer. The results of such computation are in very good agreement with the observed bow-shock shape and its surface brightness profile. We have drawn Figure 4*a* so that our slit occupies a vertical slice passing through the pulsar (which is marked with a circle at the origin). We have not convolved the models with the instrumental resolution for these images. The narrow emission core of the slow postshock gas and the broad wings of the fast postshock gas are visible in Figure 4*b* and are in good agreement with our data.

## 5. SPECTROSCOPY OF THE PULSAR COMPANION

We have performed optimal extractions of the stellar spectra at the position of PSR 1957+20 for the red and blue frames of each exposure. The total continuum fluxes were plotted as a function of pulsar phase and the excellent agreement with the light curves derived by van Paradijs et al. (1989), and DE demonstrates that we have stable flux measurements with constant contribution from the background star. This star and the pulsar companion are both believed to be of roughly spectral class G. In the top plots of Figure 5 we show the spectra of the combined flux from both objects in each spectral band. These spectra represent the sum of all exposures, weighted by signal to noise. Narrow features will be primarily due to the contaminating star since orbital variations blur those of companion to PSR 1957+20. The reduced signal to noise near the center of the red spectra is a consequence of the position-dependent frosting of the second night. The only conspicuous features are the nebular Balmer emission and an apparent absorption at 6483 Å, although significant continuum structure is evident. For comparison we plot archival spectra of the G9V standard star HD 33298. Standard stellar spectra from class mid-F through mid-K are also consistent with our observed spectra.

From the timing data of Ryba & Taylor (1992), we can estimate the companion mass and its center-of-mass line-of-sight radial velocity amplitude for an assumed pulsar mass: e.g.,

$$M_1 = 1.5\ M_\odot\ , \quad M_2 = 2.3 \times 10^{-2}/\sin i_B\ M_\odot\ ,$$
$$v_2 = 335 \sin i_B \text{ km s}^{-1}\ ;$$
$$M_1 = 1.8\ M_\odot\ , \quad M_2 = 2.6 \times 10^{-2}/\sin i_B\ M_\odot\ ,$$
$$v_2 = 355 \sin i_B \text{ km s}^{-1}\ .$$

Since the pulsar has been spun up to 1.6 ms it has accreted at least 0.1 $M_\odot$, unless it has formed directly as a fast pulsar from accretion-induced collapse of a white dwarf. The exact value of the pulsar mass (as well as that of the companion) are of course very interesting for evolutionary scenarios and would be best measured by detecting radial velocity variations of spectral lines on the companion star. Recently reported observations (Fruchter & Goss 1992) of the pulsar eclipse in the radio continuum indicate that the inclination of the orbit normal to the

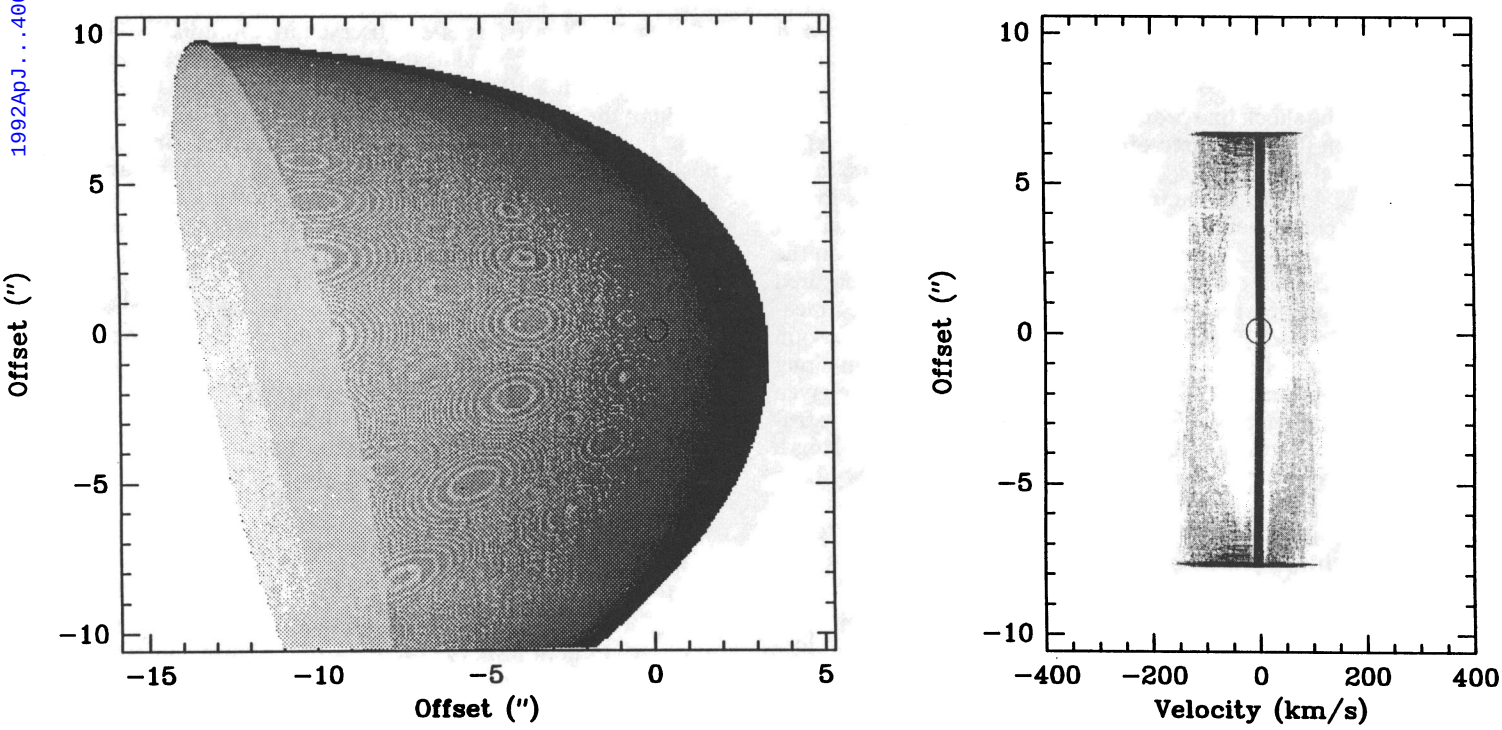


FIG. 4a

FIG. 4b

FIG. 4.—(*a*) Hα line flux image for the best-fit nebular model (see text). The bow shock has been truncated down stream from the pulsar (positioned at the open circle) to show the three-dimensional shape. No convolution for seeing has been applied. Moiré surface patterns are an artifact of the numerical binning and the color scheme. (*b*) Position-velocity cut (long-slit spectrum) in a vertical slice across the pulsar position for the best fit model shown in (*a*). No seeing or instrumental broadening has been applied. Note the narrow-line component and the broad line wings from the charge transfer postshock neutrals.

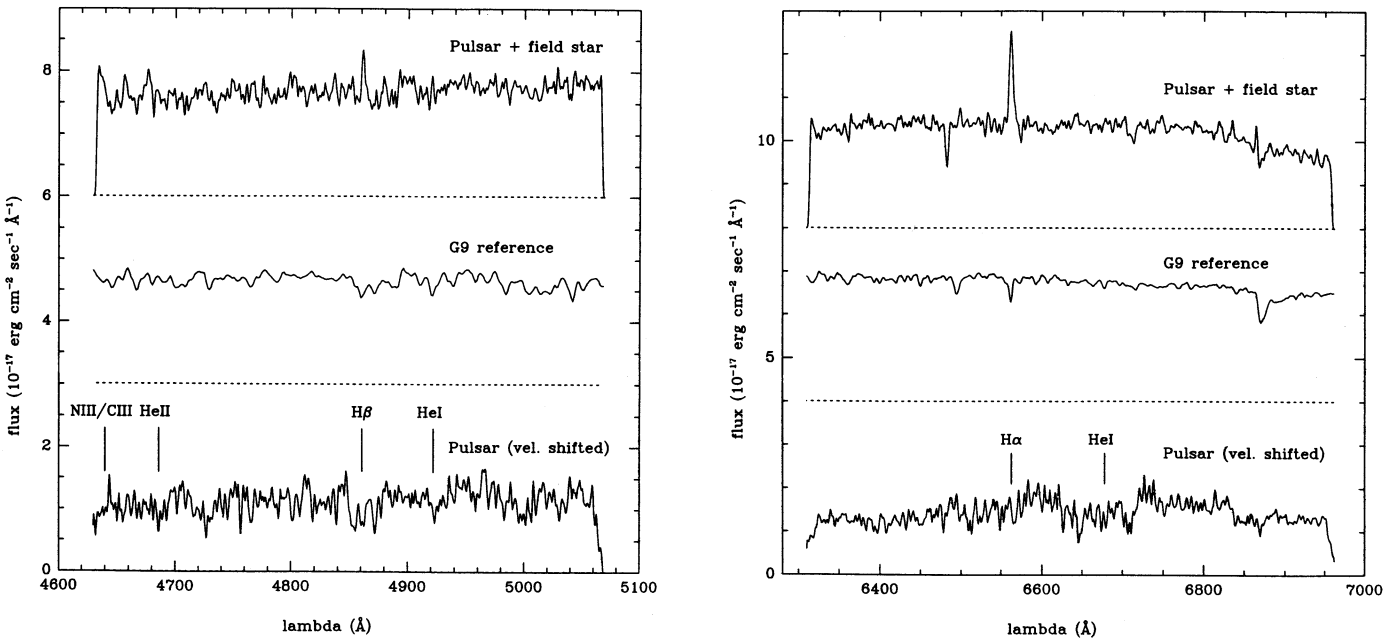


FIG. 5a

FIG. 5b

FIG. 5.—Spectra of the companion of PSR 1957+20. (*a*) Blue channel. (*b*) Red channel. *Top:* integrated spectra at the pulsar position, including the contaminating background star. *Middle:* comparison spectra of the G9V star HD 33298. *Bottom:* integrated companion spectrum after subtraction of contamination at pulsar eclipse and shifting by the expected orbital velocity.

TABLE 3

LINE LIMITS: PSR 1957+20 COMPANION

| Ion | E.W. (Å) | Flux (ergs $s^{-1}$ $cm^{-2}$) | Comments |
|---|---|---|---|
| Hα λ6563 | 0.6 | $0.8 \times 10^{-17}$ | Nebular line |
| He I λ6678 | 0.5 | $0.8 \times 10^{-17}$ | ... |
| Hβ λ4861 | 0.5 | $0.6 \times 10^{-17}$ | Nebular line |
| He I λ4922 | 0.3 | $0.3 \times 10^{-17}$ | ... |
| He II λ4686 | 0.4 | $0.4 \times 10^{-17}$ | ... |

line of sight $i_B$ is somewhat less than 90°. In any case, for $i_B \gtrsim 75°$, we expect a radial velocity amplitude close to 350 km $s^{-1}$. However, we note that the center of light of the heated companion star lies significantly inside the center-of-mass orbit; we expect its radial velocity amplitude to be reduced by ~10%.

We have derived the contaminating star spectrum from a weighted combination of spectra near minimum light and removed this from the all orbital phase observations to produce spectra of the pulsar companion. We show the companion spectrum, computed as a weighted sum of the individual spectra shifted according to the expected 350 km $s^{-1}$ motion as the lower tracings of Figure 5. Any spectral features present on the companion should remain broadened by the photospheric or wind velocity, but are in any case very weak. We place limits on the expected strong permitted lines, by measuring the local fluctuations in the continuum emission, taking 3 times the standard deviation to be a conservative upper limit. Values for both the energy flux and the equivalence width limits referred to the average companion spectrum are quoted in Table 3.

Despite difficulty in sky and background subtraction at these magnitudes, some of the continuum structure in our spectra is apparently due to normal weak photospheric line features. We have checked for variation (orbital velocity shifts) in the structure of the phase-resolved spectra by cross-correlations with standard star templates, after high-pass filtering and exclusion of the Balmer features and regions near strong sky lines. As the red spectra from 1991 July 14 have low signal to noise, the best orbital phase coverage comes from the blue data. Any orbital variations of the spectral features should be characterized by an average line-of-sight velocity $\Gamma$ and a velocity amplitude $K$. From the pulsar timing observations we know the orbital period and phase. By summing the cross correlation amplitude at the velocity expected for the orbital phase of each of our observations, we derive the combined correlation amplitude as a function of these two parameters. In this two-dimensional plane, two regions of comparably strong correlation appear at $\Gamma = -85 \pm 30$ km $s^{-1}$, $K = -10 \pm 30$ km $s^{-1}$ and at $\Gamma = 55 \pm 30$ km $s^{-1}$, $K = 300 \pm 30$ km $s^{-1}$. The former feature represents the signature of the contaminating star—since a strong peak in the simple cross correlation with the direct sum of all the spectra appears at $\sim -60$ km $s^{-1}$, we believe it is well detected. As the individual spectra are too noisy to clearly show the varying features, we regard the detection of the motions of companion to PSR 1957+20 (which would cause the second peak) as tentative. Since the combined cross-correlation analysis is affected by the features of the companion star, the velocity amplitude is somewhat suppressed and rather poorly determined. However, it is encouraging that the correlation structure appears only with the allowed phasing and with velocity amplitudes not inconsistent with those expected. Clearly, superior observing conditions and a dedicated campaign will be required to effect a precise measurement of these variations. As mentioned, the red spectra have insufficient coverage to perform this analysis. However, we note that the single strong absorption feature visible at 6483 Å is present at constant velocity throughout the observations and is absent from other nearby stellar spectra; we tentatively ascribe it to N I 6482.7, 6483.8 in the background star.

## 6. DISCUSSION

The low reddening permitted by our measured Balmer decrement as well as the ~1.2 kpc distance indicated by the best fit in our modeling have important consequences for the physics of the nebular shock and the companion wind. First, the substantial density for the ambient medium $n_0 \sim 0.4$ $cm^{-3}$ and the relatively large velocity $\gtrsim 140$ km $s^{-1}$ help insure the strong Balmer dominance and allow the shock to remain nonradiative for a substantial distance down the bow wave. The small line-of-sight velocity measured for this external medium in the postshock excitation is not surprising in view of the relatively near distance—it is interesting to note that, at least in principle, such measurements of the narrow-line components of more distant objects could give distance estimates from differential galactic rotation.

Perhaps of greater interest are the implications for the excitation of the pulsar companion. If we adopt the best-fit solution for the kinematic model, our data indicate simultaneously a substantial distance $d_{\rm kpc} \sim 1.2$ and a small extinction ($A_V$ almost certainly $< 1.0$ mag and $A_V$ probably $\lesssim 0.5$ mag). From $g$, $r$ photometry and light curve modeling DE argue that the companion radius is $\log R_c = \log d_{\rm kpc} - 0.126 A_V + 10.21$. This is to be compared with the volume equivalent Roche radius, which for $M_{\rm psr} = 1.5\ M_\odot$ is $2.0 \times 10^{10}$ cm. With DE's estimate the system will be in contact for $d_{\rm kpc} \gtrsim 1.2$ ($A_V = 0$) or $d_{\rm kpc} \gtrsim 1.4$ ($A_V = 0.5$). Thus, in particular for the lower $A_V$, our data indicate that the companion is probably close to filling its Roche lobe. We note that recent reassessment of the dispersion measure scale, as well as the difficulty of exciting a strong radiation-driven wind have led others to similar conclusions (e.g., Fruchter & Goss 1992; Levinson & Eichler 1991).

However, the precise value for the distance fit depends on the velocity field in the postshock layer, the extent of mixing in the flow around the bow wave, the fraction of the line in the broad component, and to a lesser extent the detailed shape of the shock wave. If the flow more closely follows the well-mixed, thin shock solution, the implied distances are somewhat smaller. Higher resolution observations, more extensive spatial coverage of the nebular and improved hydrodynamic models of the shocked layers are required to provide a clean measurement of $d_{\rm kpc}$. Despite the uncertainties, we wish to highlight that the kinematic method for determining the distance from nebular spectroscopy described here offers the best hope for resolving this important question. Noise in this radio pulsar and its faintness made it unlikely that a conventional parallax can be determined for this object.

Our bounds on line emission in the companion stellar photosphere are also important for understanding its excitation by the pulsar. For a limit on the line strength of $\lesssim 10^{-17}$ ergs $cm^{-2}$ $s^{-1}$ and an excited region of the companion star of size $\sim 1.5 \times 10^{10}$ cm, the surface emissivity of lines in our optical range is $F_{*,L} \lesssim 2 \times 10^6 d_{\rm kpc}^2$ ergs $cm^{-2}$ $s^{-1}$. Levinson &

Eichler have emphasized that for low incident radiation fields, as for the companion of PSR 1957+20, line cooling above the continuum photosphere will be important in limiting the effective temperature available to drive a thermal wind. They estimate that the maximum temperature attainable for PSR 1957+20's parameters is $\sim 7 \times 10^4$ K; for this temperature an optical $\lambda \sim 5000$ Å thermalized line would then have a surface flux $\sim 10^9$ ergs cm$^{-2}$ s$^{-1}$, from their estimates. Clearly, our limits on lines (for several ionization states) are much lower than this value. Indeed, our line flux limits are comparable to the nominal fluxes of the $\sim 5000$ K effective stellar temperature estimated by DE; of course, an atmosphere at such a temperature would lack optically thick emission lines and would instead exhibit the normal weak metal absorption features probed in our cross correlation analysis.

These rather stringent limits on optically thick lines at high coronal temperatures pose severe difficulties for thermally driven winds. For significant mass flux with temperatures of less than $10^4$ K the stellar photospheric radius must be more than 90% that of the Roche lobe. This requires distances $d_{\rm kpc} \gtrsim 1$, even with the low $A_V$ implied by the Balmer decrement. The pulsar heating of the companion atmosphere may be then quite important in driving a high mass-loss rate over the remaining low potential barrier. The momentum in the pulsar wind may also be an important ingredient in effecting the ablation. The required large distance is in good agreement with our modeling if $f_b$ is less than the theoretically preferred value of $\frac{2}{3}$. One likely source of the additional narrow-line flux is photoionization and/or suprathermal electron preheating of the ISM upstream of the pulsar wind shock. Separation of this flux from the bow-wave shock front, as well as resolving the nonradiative emission from the bow-wave apex (which should extend $\sim 1''$) may require HST imaging. The best hope for resolving this question with ground-based facilities lies in higher resolution Echelle spectroscopy or Fabry-Perot imaging of the bow-shock emission. An improved isolation of the broad line strength and better measurement of the velocity width should allow high precision for the kinematic distance determination. Also Fabry-Perot imaging would allow the study of nonradiative shock excitation for a variety of effective velocities, due to the varying obliquity of the box shock nebula. Another significant variation from our assumptions would occur if the pulsar moment of inertia were much larger than the expected $I_{45} \sim 1$. Note that, in principle, higher resolution observations along with shock modeling estimates of the upstream ISM density could allow this interesting quantity to be separately constrained. Also if the narrow-line contribution is indeed in excess of simple shock estimates, then a measure of its width could confirm the presence of preheating and line emission and would further constrain the shock physics. A large telescope and an efficient spectrograph would be required for this task.

## 7. SUMMARY

We have acquired phase-resolved long slit spectra of the binary pulsar PSR 1957+20 and the surrounding bow shock nebula. Our results can be summarized as follows:

1. In the spectra of the bow-shock nebula, we clearly detect the H$\alpha$ and H$\beta$ lines, but the lines of heavier species were not seen. We set upper limits on these line strengths as 3.5% of the H$\alpha$ flux in the red spectral range and 16% of the H$\beta$ flux in the blue range. This strong Balmer dominance implies that the shock is nonradiative.
2. We have measured the H$\alpha$/H$\beta$ flux ratio to be $3.5 \pm 0.5$. This low value is in agreement with estimates for slow nonradiative shocks and implies a small visual absorption $A_V \lesssim 1$ mag.
3. We develop a numerical model for the H$\alpha$ line profile of the bow-shock nebula which is specified by five parameters. By fitting this model to the observed long-slit spectrum we determined these parameters, the most important of which is the distance to the pulsar $d_{\rm kpc} \approx 1.2$. Our data imply that the pulsar companion is close to filling its Roche lobe.
4. We have performed optimal extractions of the spectra at the position of PSR 1957+20 and find no emission lines indicative of strong heating in the companion wind. However, a velocity cross-correlation analysis against templates of late-type dwarf photospheric spectra was sensitive to weak photospheric absorption features. We find a peak at an orbital velocity amplitude of $K = 300 \pm 30$ km s$^{-1}$, phased with the expected companion motion. The identification with the companion radial velocity is tentative but suggests promise for more extensive observations.

We thank Scott Lundgren for help in the data acquisition, Juan Carasco and Dave Tennant for assistance with the observations and the instrumentation, Vicki Johnson for help with data reduction and Mordecai-Mark MacLow, Chris McKee, and David Eichler for helpful discussions on the geometries of bow shocks and on pulsar wind physics. Observations at Palomar Observatory were made as part of a collaborative agreement between the California Institute of Technology and Cornell University. R. W. R. was supported in part by grant NAGW-2963, while J. M. C.'s research was partly supported by the National Astronomy and Ionosphere Center.

## REFERENCES

Baranov, V. B., Krasnobaev, K. V., & Kulikovskii, A. G. 1971, Soviet Phys., 15, 791
Djorgovski, S., & Evans, C. R. 1988, ApJ, 335, L61 (DE)
Fruchter, A. S., & Goss, W. M. 1992, ApJ, 384, L47
Fruchter, A. S., Stinebring, D. R., & Taylor, J. H. 1988, Nature, 333, 237
Gunn, J. E., & Oke, J. B. 1983, ApJ, 266, 713
Kluzniak, W., Ruderman, M., Shaham, J., & Tavani, M. 1988, Nature, 334, 225
Kulkarni, S., Djorgovski, S., & Fruchter, A. S. 1988, Nature, 334, 524
Kulkarni, S. R., & Hester, J. J. 1988, Nature, 335, 801 (KH)
Levinson, A., & Eichler, D. 1991, ApJ, 379, 359
Mac Low, M.-M. M., van Buren, D., Wood, D. O. S., & Churchwell, E. 1991, ApJ, 369, 395
McKee, C. F., & Hollenbach, D. J. 1980, ARA&A, 18, 219
Oke, J. B., & Gunn, J. E. 1982, PASP, 94, 586
Phinney, E. S., Evans, C. R., Blandford, R. D., & Kulkarni, S. R. 1988, Nature, 333, 832
Press, W. H., & Teukolsky, S. A. 1991, Comput. Phys., 5, 426
Raymond, J. C. 1991, PASP, 103, 781
Raymond, J. C., Blair, W. P., Fesen, R. A., & Gull, T. R. 1983, ApJ, 275, 651
Raymond, J. C., Davis, M., Gull, T. R., & Parker, R. A. R. 1980, ApJ, 238, L21
Romani, R. W. 1990, Nature, 347, 741
Ruderman, M., Shaham, J., & Tavani, M. 1989, ApJ, 336, 507
Ryba, M. F., & Taylor, J. H. 1992, ApJ, submitted
Van Buren, D., & Mac Low, M.-M. M. 1992, preprint
van Paradijs, J., et al. 1988, Nature, 334, 684